Available at www.sciencedirect.com

ScienceDirect

journal homepage: www.elsevier.com/locate/he

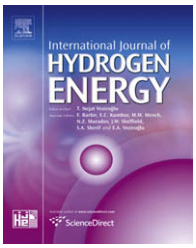

Kinetic investigation of hydrogen generation from hydrolysis of SnO and Zn solar nanopowders

Marc Chambon, Stéphane Abanades, Gilles Flamant*

Processes, Materials and Solar Energy Laboratory (CNRS-PROMES), 7 Rue du Four Solaire, 66120 Font-Romeu, France

ARTICLE INFO

Article history:
Received 18 February 2009
Received in revised form
20 April 2009
Accepted 28 April 2009
Available online 30 May 2009

Keywords:
Hydrogen
Water-splitting
Solar energy
Kinetics
Tin oxide
Zinc
Nanoparticles

ABSTRACT

The hydrolysis reaction of the two-step ZnO/Zn and SnO_2/SnO thermochemical cycles was kinetically investigated for solar hydrogen production. Nanoparticles of Zn and SnO were synthesized by solar thermal reduction of the oxides and neutral gas quenching of the vapors. They were then hydrolyzed to quantify and compare the H_2 yields and the kinetic rate laws in fixed-bed. The hydrolysis of Zn nanoparticles reached only up to 55% of H_2 yield, whereas SnO hydrolysis was almost complete. In contrast, Zn hydrolysis was much faster than SnO hydrolysis, but Zn deactivation occurred suddenly. Models of solid–gas reactions were applied to identify the controlling mechanisms and the associated kinetic parameters. The kinetic models were fitted to both isothermal and non-isothermal (temperature ramp) hydrolysis experimental data. Activation energies and reaction orders were found to be 122 ± 13 kJ/mol and 2.0 ± 0.3 for SnO, and 87 ± 7 kJ/mol and 3.5 ± 0.5 for Zn, respectively. Finally, a shrinking core approach was applied to the case of SnO to account for the reaction-controlling mechanisms.

© 2009 International Association for Hydrogen Energy. Published by Elsevier Ltd. All rights reserved.

1. Introduction

With oil era foreseen to come to an end shortly, mankind has no choice but to widen its search for alternative energy sources in order to keep its technological development sustainable [1]. This background and the environmental urge for reducing the CO_2 emissions have stressed the hydrogen economy concept [2]. Thermochemical water-splitting cycles are promising routes to produce clean hydrogen with high-temperature renewable heat and water as only inputs. Given an M_xO_y/M_xO_{y-1} redox system, a two-step cycle is defined by the separate reactions below [3]

$$\text{High-temperature reduction}: \quad M_xO_y \rightarrow M_xO_{y-1} + 1/2O_2 \ (\text{endothermal}) \qquad (1)$$

$$\text{Low-temperature hydrolysis}: \quad M_xO_{y-1} + H_2O \rightarrow M_xO_y + H_2 \ (\text{exothermal}) \qquad (2)$$

Concentrated solar energy can be used for high-temperature heating [4]. Among the first investigated solar-driven cycles, the ZnO/Zn cycle is defined as a volatile oxide cycle because the reduction step occurs with the decomposition of ZnO into gaseous products ($Zn_{(g)}$ and O_2) [5]. Dilution/quenching with a neutral gas at the reactor exit avoids parasitic reverse oxidation [6] and yields nanoparticles of reduced species (Zn) by condensation [7]. Zinc reacts with water at a temperature close to its melting point (693 K) by producing pure H_2 and forming back the original zinc oxide. Steam hydrolysis of molten zinc was first considered [8]. However, the produced ZnO layer hinders the diffusion processes between the surface and the internal zinc, and thus stops the

* *Corresponding author*. Tel.: +33 4 68 30 77 30; fax: +33 4 68 30 29 40.
E-mail address: stephane.abanades@promes.cnrs.fr (S. Abanades).

0360-3199/$ – see front matter © 2009 International Association for Hydrogen Energy. Published by Elsevier Ltd. All rights reserved.
doi:10.1016/j.ijhydene.2009.04.064

Nomenclature

A_0	pre-exponential factor (model-dependent unit)
α	chemical conversion
β	heating rate, K/min or K/s
C_i	molar concentration of compound i, mol/m^3
D_e	H_2O diffusivity in the oxide layer, m^2/s
E_a	activation energy, kJ/mol
F_i	molar flow-rate of compound i, mol/s
f_{wt}	mass fraction of reduced species in the powder, wt%
k	kinetic constant, s^{-1}
l	relative weight loss
M_i	molar weight of compound i, g/mol
m	mass of powder from solar thermal reduction, g
N_i	mole amount of compound i, mol
n	reaction order
P, P_i	total pressure or partial pressure of i, Pa
Q_i	volumetric flow-rate of compound i, NL/min
R	ideal gas constant 8.314 J/K/mol
r	mean particle radius, m
ρ_i	density of compound i, kg/m^3
$\rho_{m,i}$	molar density of compound i, mol/m^3
T	temperature in the reactor, K
t	hydrolysis duration, s
V_M	molar volume at normal conditions 22.4 NL/mol
x_i	mole fraction of compound i, mol%

hydrolysis. Consequently, zinc powders with high surface-to-volume ratio, including nanoparticles produced via Zn evaporation and condensation of Zn vapors, were used to bypass this diffusion-related issue [9–14]. Recently, the SnO_2/SnO redox couple was demonstrated to be an efficient two-step cycle [15–17] that shares many characteristics with the ZnO/Zn system, such as (1) the vapor phase products in the solar step, (2) the similar reduction temperature range (about 2073 K at atmospheric pressure), (3) the need for neutral gas dilution and quenching in step 1 to avoid reverse oxidation, and (4) the solar synthesis of reduced particles in the nanometer size range if the quenching is fast enough.

This study focuses on the hydrolysis reaction yielding hydrogen from water-splitting. The kinetics of SnO hydrolysis was never studied but only considered as an intermediate step of the metallic tin hydrolysis [18,19]. The hydrolysis of solar zinc, i.e. Zn nanoparticles synthesized from purely solar thermal reduction of ZnO, was neither investigated in detail. Previous studies on zinc particle hydrolysis have only been performed either with commercial zinc powders [11,14] or with zinc obtained from solar carbo-reduction of ZnO [10]. The conversion observed in an aerosol flow reactor fed with water vapor and commercial Zn particles (average size of 158 nm) was about 24% at 813 K and a gas residence time of about 0.6 s [11]. Non-isothermal thermogravimetric analysis (TGA) with dispersed Zn powder on quartz wool indicated that complete Zn conversion could be achieved for longer residence times. Concerning Zn from solar carbo-reduction, increasing the temperature of steam flow injection from 473 to 823 K improved the Zn conversion from 24% to 81% during the fast stage (observed from 673 K) [10]. Besides, other hydrolysis studies also involved the intermediate Zn evaporation before steam-quenching the vapors to co-produce H_2 and Zn/ZnO nanoparticles [12,13], but this method suffered from low particle yield and significant wall deposition.

These studies showed strong discrepancies in the estimated activation energy of Zn hydrolysis, ranging from 132 kJ/mol [11] to 43 kJ/mol [14], despite the use of sub-micron Zn powders (same purity and supplier) and similar methodologies for determining the kinetic parameters (thermogravimetry). These differences in activation energy can be explained by the preparation methods and morphology of the reacting particles. Moreover, all the considered initial reactant powders were only slightly oxidized, whereas the powders from solar reduction exhibit significant oxide content due to the presence of oxygen during synthesis, which may modify the particles morphology [7] and reactivity [9]. These reasons motivated a new kinetic study for Zn hydrolysis based on solar-produced powders. The ultimate goal of this approach was to provide a fair comparison of the hydrolysis step for solar Zn and SnO prepared with common synthesis conditions.

In this study, nanoparticles of Zn and SnO were produced via purely solar thermal reduction and neutral gas quenching with the same device and operating conditions, in order to obtain reliable and comparable results on the hydrolysis step. The hydrolysis of the Zn and SnO solar-produced nanopowders was investigated to quantify and compare the H_2 yields and the kinetic rate laws. Models of solid–gas reactions were applied to identify the controlling mechanisms and the associated kinetic parameters.

2. Experimental section

2.1. *Solar synthesis of nanopowders and characterization*

The SnO and Zn nanoparticles were produced from compressed powders (0.5–1.0 g pellets) in a previously described solar experimental set-up [17], except that the refrigerant device was pulled out in order to only perform a gaseous quenching and thus simplify the synthesis conditions. Reduced pressure (115 ± 5 mbar) was selected because it favors both thermodynamics and kinetics, and it limits the parasitic recombination by decreasing the oxygen partial pressure [16]. Gas flow regime was set to laminar to avoid backflows of oxygen-rich gas near the reduction area. This was performed by choosing an appropriate nitrogen flow-rate (1.5 NL/min) for quenching/dilution and by controlling the solar heat flux. The duration of the reduction reaction and the weight of the reactive oxide before and after the reaction allowed the calculation of the mass loss per minute. This provided an estimation of the reduction temperature based on previous kinetic studies [16]. The maximum dilution ratio was defined as the mole ratio between the flow-rate of neutral gas and the flow-rates of produced oxygen and reduced oxide vapor. An overview of the synthesis conditions (average of 10

runs) is summed up in Table 1. Each solar reduction experiment (15–30 min) gave about 100 mg of powder. The mass fraction f_{wt} of reduced species (Zn or SnO) in the recovered powder was defined as follows:

$$f_{wt} = \frac{m_{red}}{m_{red} + m_{ox}} \quad (3)$$

where $m = m_{red} + m_{ox}$ is the total mass of powder composed of the reduced species and the oxide formed via recombination with oxygen. The mass fraction of reduced species f_{wt} ranged from 65% to 90% (estimated by calibrated XRD using standards of known concentration [20]), with 5% of relative uncertainty for both SnO and Zn [16]. Crystallite sizes of the reduced species, estimated from the Scherrer's equation [21], were 22 ± 5 nm and 26 ± 5 nm for SnO and Zn, respectively. True density of the powders was estimated from Eq. (4) by neglecting structural variations of the crystallographic structures at the oxide/reduced oxide interfaces.

$$\rho = \frac{1}{\frac{f_{wt}}{\rho_{red}} + \frac{1 - f_{wt}}{\rho_{ox}}} \quad (4)$$

True densities of SnO and Zn powders were 6550 ± 50 kg/m^3 and 6730 ± 120 kg/m^3, respectively, according to their f_{wt}. Bulk densities of solar-produced SnO and Zn nanopowders were estimated as 220 ± 20 kg/m^3 and 700 ± 50 kg/m^3, respectively (weighed graduated vial with volume measured after vibrations), and gave void fractions of $97 \pm 1\%$ and $91 \pm 1\%$. For both powders, scanning electron microscopy (SEM) showed heterogeneous agglomerates (1–50 μm) of nanoparticles (Fig. 1(A1) and (B1)). The high void fractions suggest (if open porosity) that these agglomerates contain a lot of interstitial spaces allowing internal steam diffusion. The reduced SnO powders consisted of disk-shaped SnO nanoparticles (about 100 nm diameter and 20 nm thick) [22] and nanoentities (Fig. 1(A2)). The agglomerates obtained from ZnO solar thermal reduction contained ZnO tetrapods/needles [23] (about 20 nm diameter and 100 nm length) that were formed during recombination with O_2, but the zinc nanoparticles themselves produced from ZnO solar dissociation were not similar to those of previous studies (involving Zn evaporation and steam-quenching of Zn vapor in aerosol flow reactors), since hexagonal-shaped or spherical entities were not observed [7,13] (Fig. 1(B2)).

The particle morphology can change during the hydrolysis. This is especially true for Zn as fast hydrolysis occurs near its melting point, and thus sintering may occur. Consequently, the powders were observed through environmental SEM (ESEM). The powder produced from solar thermal reduction (2–5 mg as stacked agglomerates) was placed in a steam atmosphere (vacuum required, saturated with steam: $P = P_{H_2O} = 2.4$ mbar) on a heating sample holder (20 K/min up to 673 K and then 5 K/min up to 773 K). The ESEM beam was focused on a given agglomerate for the whole reaction duration. No extra-sintering or agglomerate breaks were observed on the Zn and SnO agglomerates at micro-scale. The H_2 release results in the disturbances of the beam, so it was not possible to dynamically follow changes at the nano-scale. However, classic SEM was performed on the ESEM-hydrolyzed powders. It showed some cracks on the nanodisks of SnO powder (Fig. 2). These cracks were not observed on particles hydrolyzed in the fixed-bed reactor. This may come from the different reaction conditions in ESEM (low pressure and steam amount in particular), causing high constraints inside the SnO nanodisks during H_2 release. No visible change was noted for the Zn powder at the 100 nm scale. The absence of sintering/melting for Zn can be explained by the produced ZnO layer wrapping Zn nanoentities and stopping their merging [11]. Furthermore, the solar-produced Zn powder is dispersed and contains an initial amount of oxide, which also explains the absence of conglomerates and melted zinc fragments after the hydrolysis. Experiments were then conducted to characterize the hydrolysis step in a fixed-bed reactor and to determine kinetic rate laws.

Table 1 – Operating conditions of nanopowder synthesis by solar thermal reduction at P = 115 mbar.

	Fraction of mass loss per minute (%/min)	Estimated reduction temperature (K)	Maximum dilution ratio
SnO_2	2 ± 1	1820 ± 50	480 ± 240
ZnO	1.0 ± 0.5	1640 ± 50	560 ± 280

2.2. *Hydrolysis reactor*

The reactor featured a fixed-bed of reactive particles heated in a tubular furnace. It is described in detail in Refs. [16,17]. The heating elements were controlled by a programmable regulator (STATOP 4849 Chauvin Arnoux) and could heat linearly. The temperature of the bed was measured by a K-thermocouple in contact with the particles. Steam was generated upstream in an independent furnace and was carried to the bed by an argon flow ($Q_{Ar} = 0.18$ NL/min). The output gases went through a water trap and a drier (Drierite™) before entering a catharometric analyzer (ARELCO Catarc 10P calibrated with 10% H_2 in argon, detection limit: 100 ppm, precision: 1% of full scale, scales used: 0–5% for SnO and 0–10% for Zn) [16,17]. The H_2 mole fraction was thus measured continuously. The response time between the bed and the analyzer was about 15–25 s. The sample holder consisted of a removable stainless steel tube (10 mm i.d.) with an iron grate support at the bottom (sieve void: 100 μm). A layer of dry silica sand (0.5 g, diameter: 0.4–0.5 mm) was first spread, and the powder was then sprinkled over it (95 ± 10 mg, reduced oxide fraction: 65–90 wt%). This arrangement minimized reactive particle losses caused by the carrier gas. No significant pressure drop through the bed was observed (a manometer measured the pressure before the fixed-bed reactor). Steam flow-rate was controlled with a peristaltic pump that injected liquid water at a fixed rate of 0.05 ± 0.01 g/min. Consequently, the total gaseous flow contained 26 ± 5 mol% of steam (steam partial pressure: 22 ± 4 kPa, reactor pressure: 85 kPa). Before the start of the hydrolysis, the peristaltic pump was operated reversewise for a dozen of minutes to purge the injection tube with argon. The tubular section between the two furnaces was wrapped up with insulating material (ceramic fiber) to avoid condensation. This set-up was used for performing (1) isothermal hydrolysis tests by injecting steam when the reactor temperature reached the set-point (about 5 min to

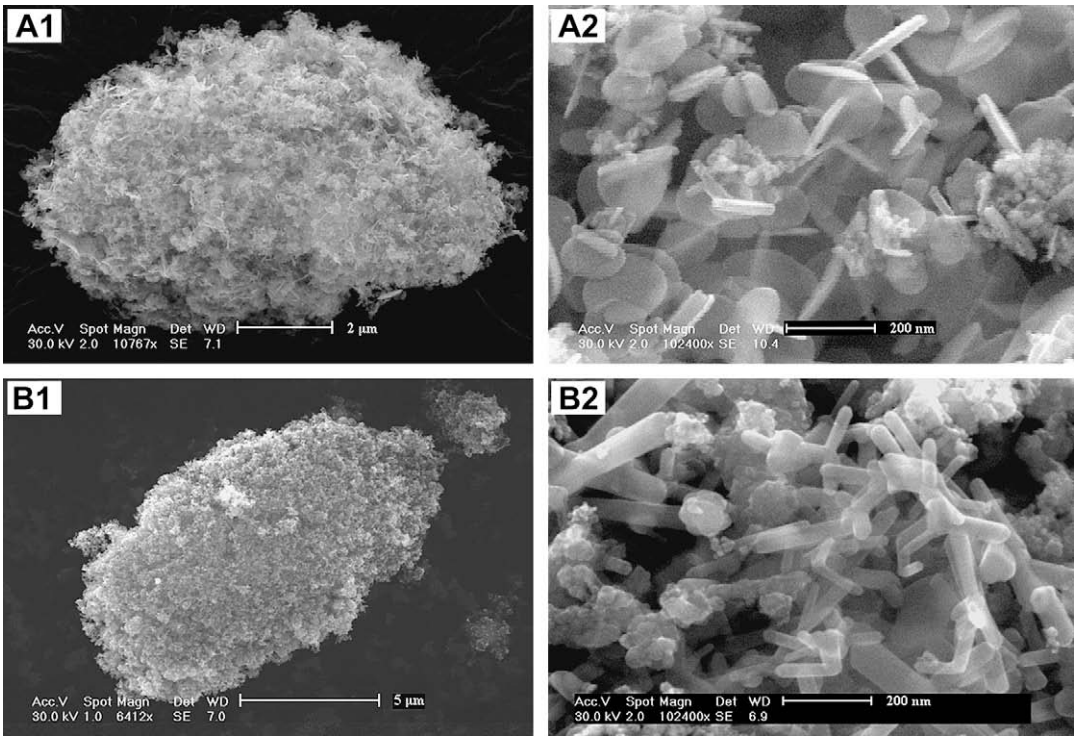
A1
Acc.V Spot Magn Det WD 2 µm
30.0 kV 2.0 10767x SE 7.1
A2
Acc.V Spot Magn Det WD 200 nm
30.0 kV 2.0 102400x SE 10.4
B1
Acc.V Spot Magn Det WD 5 µm
30.0 kV 1.0 6412x SE 7.0
B2
Acc.V Spot Magn Det WD 200 nm
30.0 kV 2.0 102400x SE 6.9

Fig. 1 – SEM pictures at micro- and nano-scales of (A) SnO and (B) Zn powders obtained from solar thermal reduction and gaseous quenching.

reach steady state); and (2) non-isothermal hydrolysis tests by setting a constant heating rate and by injecting steam at the temperature for which hydrolysis becomes noticeable.

The bed temperature and H_2 mole fraction x_{H_2} were monitored and recorded every half a second. The final flow only contained H_2 and argon because water was trapped before the analyzer thanks to the gas drying unit. Consequently, the H_2 molar flow-rate (mol/s) is given by (ideal gas law)

$$F_{H_2} = \frac{x_{H_2}}{1 - x_{H_2}} \cdot F_{Ar} \tag{5}$$

where $F_{Ar} = Q_{Ar}/V_M$.

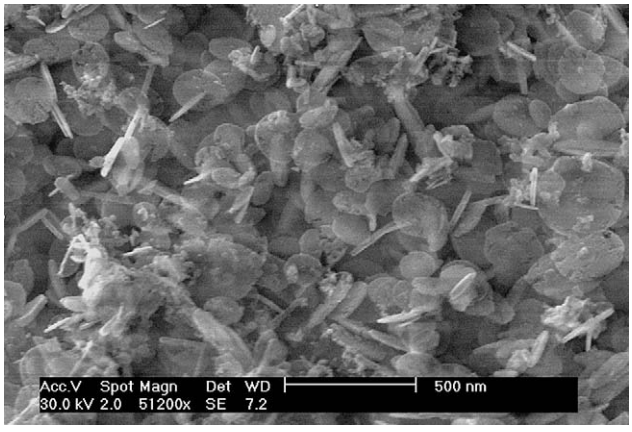

Fig. 2 – Surface of SnO agglomerates after hydrolysis in ESEM.

The total amount of produced hydrogen N_{H_2} (mol) is calculated through a standard numerical integration given the low time step ($\Delta t = 0.5$ s)

$$N_{H_2} = \sum_{t_i}^{t_f} F_{H_2} \cdot \Delta t \tag{6}$$

Finally, the conversion or H_2-yield α is as follows:

$$\alpha = \frac{N_{H_2} \cdot M_{red}}{m \cdot f_{wt}} \tag{7}$$

where m is the mass of powder in the reactor.

The relative weight loss l of powder during hydrolysis is estimated from the following equation:

$$l = \frac{m \cdot \alpha \cdot f_{wt} \cdot \left(\frac{M_{ox}}{M_{red}} - 1\right) - \Delta m}{m} \tag{8}$$

where Δm is the mass variation of the removable sample holder. It was 4% (average of 8 runs with no significant difference between the Zn and SnO powders, max 6%) for a 1 h flushing time including the hydrolysis duration. Such relative weight losses were similar to those estimated in other fixed-bed experiments [10] and were neglected in the study.

3. Results and discussion

3.1. *Qualitative comparison of Zn and SnO hydrolysis*

First, isothermal experiments were performed with SnO and Zn solar-produced powders. The amount of hydrogen

detected in the outlet gas suddenly increased when water was injected. As a result, a peak in H_2 mole fraction was observed about 25 s after the steam was injected and the maximum H_2 flow-rate increased with temperature (Fig. 3). Therefore, the conversion curves should theoretically present the characteristic inflexion points, but they were not visible because of the short time lag between steam injection and maximum H_2 detected in the off-gas. Practically, the conversion rate increased markedly at the time of steam injection (Figs. 4 and 5). The hydrolysis reaction showed a fast step before the conversion gradually leveled-off, which is typical of solid–gas reactions with an oxide layer growing at the particle surface. This result suggests a reaction-controlled regime during the fast step, and then a diffusion-controlled regime which accentuates while the oxide product forms at the surface. The fast step lasted several minutes in the case of SnO, whereas it was short for Zn (less than 1 min) and the reaction stopped suddenly in the latter case despite the nano-sized powders. The reaction rate becomes negligible because a low-permeable zinc oxide layer is formed at the surface of the particles and grows with time, which hinders the reaction [14]. In the case of Zn hydrolysis, a temperature peak occurred during the fast step because of the high reaction rates coupled with the high reaction enthalpy (−110 kJ/mol for Zn and −49 kJ/mol for SnO at 773 K). The experiments were performed with small amounts of powders (100 mg) to avoid excessive overheating of the sample. Hence, an increase in the bed temperature limited to about 5 K was measured in every zinc hydrolysis tests.

The isothermal experiments pointed out strong differences in SnO and Zn behaviors. The hydrolysis of solar-produced SnO was slow but the reaction nearly approached completion, whereas the hydrolysis of solar-produced Zn was quick, but the H_2 production stopped abruptly and the particles reacted partially (Fig. 5). Indeed, the conversion reached 80% for SnO half-an-hour after the steam injection at about 800 K, but Zn conversion stopped in the best case at 55%.

The last noteworthy feature concerned the hydrogen content that was measured before the steam injection. The powders produced hydrogen during the heating period before feeding water. Given the argon with high purity, this reaction

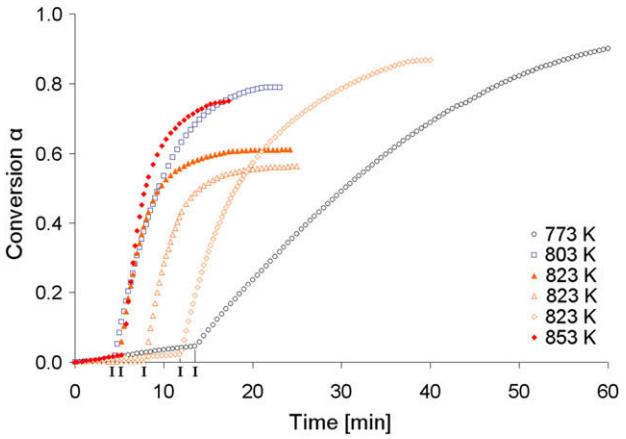

Fig. 4 – Hydrolysis of solar-produced SnO powders (isothermal) with steam injections starting at times *I*.

can only be explained by adsorbed water or hydroxyl species. However, the amount of hydrogen generated before steam injection was much higher in the case of zinc powders and the corresponding conversion reached 15–20% (it was limited to a few percent for SnO). This was repeated with freshly solar-produced zinc powder (2 h between the solar synthesis and hydrolysis, 40–50% of relative humidity) without significant difference. A particular test was carried out at 748 K (Fig. 5) to quantify the maximum H_2 production without steam injection and a final yield of up to 30% was reached. At this time, steam was injected but the amount of further H_2 released was negligible. Isothermal hydrolysis experiments were thus less suited for kinetic studies in the case of Zn because the powders had partly reacted before the targeted temperature was reached.

Then, non-isothermal hydrolysis tests were performed at different heating rates. Steam was injected as soon as the powders reactivity was detected (553 K for Zn and 693 K for SnO). The reactor temperature increase during hydrolysis allowed complete kinetic characterization with a single experiment [11], which cancelled the uncertainties

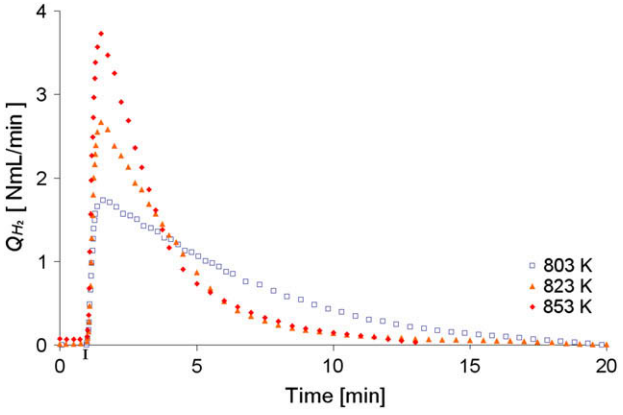

Fig. 3 – Evolution of H_2 flow-rate during the hydrolysis of solar-produced SnO powders (isothermal) with steam injection starting at time *I*.

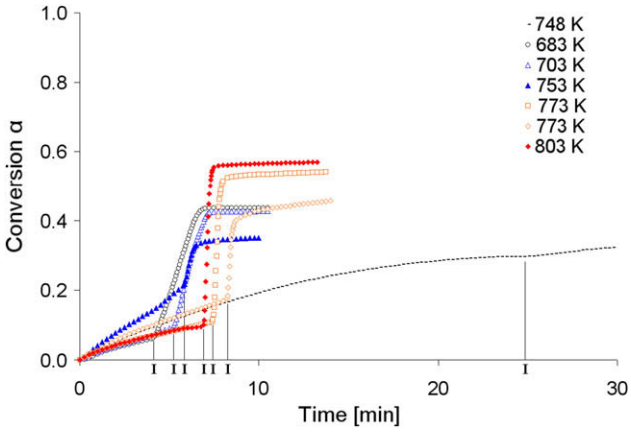

Fig. 5 – Hydrolysis of solar-produced Zn powders (isothermal) with steam injections starting at times *I*.

encountered in isothermal hydrolysis due to compositional variations between samples. Figs. 6 and 7 show the time course of conversions and temperatures for SnO and Zn hydrolysis performed at different heating rates. The temperature-dependent reaction rate was controlled by the linear heating rate and an inflexion point was observed on the conversion versus time profiles (Figs. 6 and 7). At this point, the conversion rate started to significantly slow down and the reaction-controlled regime moved to the diffusion-controlled regime. The final conversion was below 50% for Zn and did not increase anymore while temperature continued to rise. Inversely, SnO conversion was almost complete. The low conversion rates for Zn agreed with previous studies. Indeed, nearly complete conversions were only observed with highly dispersed nanoparticles (instead of agglomerates) [11] or with crackling zinc particles at temperatures higher than 800 K [10].

The powders that were recovered after hydrolysis did not show any sintering evidence according to SEM pictures. In the case of Zn, however, the switch to the diffusion-controlled regime followed by the sudden Zn deactivation took place near Zn melting point (about 700 K, Fig. 7). This may be due to the sintering inside the agglomerates, although the void fractions did not change significantly after the hydrolysis (still above 90%).

3.2. *Kinetic models for hydrolysis reactions*

3.2.1. *Kinetic fitting based on isothermal hydrolysis*

Following a classical approach, the kinetic equation was assumed to have the following uncoupled form [11]

$$\frac{d\alpha}{dt} = A_0 \cdot e^{-E_a/RT} \cdot f(\alpha) \quad (9)$$

where $f(\alpha)$ is a model-dependent depletion term. It equals unity at the beginning of steam injection if there is no diffusion limitation, and it is null when the conversion stops. The kinetics was first identified from the hydrolysis data of Fig. 4 related to SnO powders prepared from solar thermal reduction with a simple gas quenching. Assuming no diffusion limitation at the beginning of the hydrolysis, a logarithmic plot of the initial conversion rate (taken at the time of steam injection) versus 1/RT gave an activation energy of 124 ± 15 kJ/mol for SnO ($R^2 = 94\%$, Fig. 8). This activation energy was higher than the one previously reported in Ref. [16] (67.4 kJ/mol,

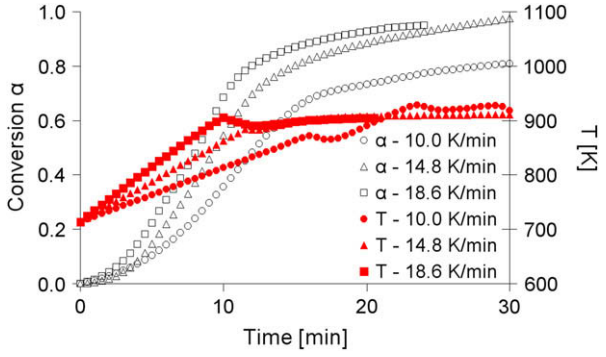

Fig. 6 – Hydrolysis of solar-produced SnO powders (non-isothermal) at different heating rates.

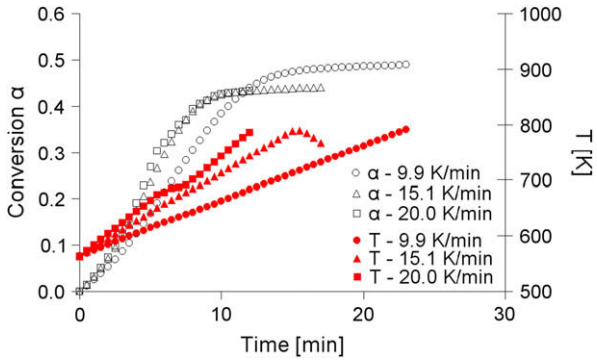

Fig. 7 – Hydrolysis of solar-produced Zn powders (non-isothermal) at different heating rates.

$R^2 = 99\%$) for powders synthesized with fast quenching. This shows the influence of quenching on the kinetic parameters. The fast quenching limits the recombination of SnO with O_2 (f_{wt} above 90%), which thus reduces the thickness of the initial SnO_2 layer at the particle surface. Then, the reactant transfer is not hindered, which facilitates the surface reaction and lowers the apparent activation energy. Furthermore, the quenching stops the particle growth process and may globally result in lower particle size, which also explains the decrease of activation energy, as discussed in Ref. [14].

In the case of solar-produced Zn, an activation energy of 87 ± 7 kJ/mol was found from the hydrolysis data of Fig. 5 ($R^2 = 98\%$, Fig. 8). The conversion before steam injection was significant in the case of zinc (15–20%) because of residual adsorbed water, which means that a ZnO layer was formed before the start of the injection. However, similar to the case of SnO, the initial conversion rate ($d\alpha/dt$) used in the fitting was the slope of the conversion curve at the time of steam injection. The above activation energies were estimated from the initial reaction rates (rate of conversion increase) of the isothermal tests when diffusion limitation is not the controlling step.

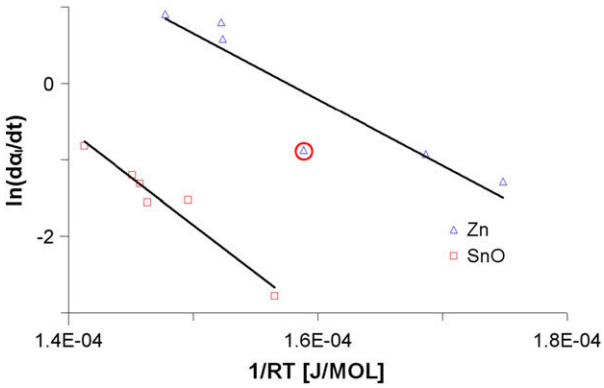

Fig. 8 – Logarithm of the initial conversion rate versus 1/RT for powder hydrolysis ($E_a = 124 \pm 15$ kJ/mol, $R^2 = 94\%$ for SnO and $E_a = 87 \pm 7$ kJ/mol, $R^2 = 98\%$ for Zn). Data point circled in red was not considered in the regression (it corresponds to the isothermal hydrolysis at 753 K with an initial Zn conversion before steam injection at 20% versus 10–15% for the other Zn powders).

It is commonly assumed that the oxide layer appearing on the particles during the hydrolysis hinders the reaction. Thus, the higher the conversion, the lower the kinetic rate. This can be translated in Eq. (9) by an empirical depletion term $f(\alpha) = (1-\alpha)^n$, where n is the reaction order. Then, the reaction order and pre-exponential factor were identified by integrating Eq. (9) between the injection and time with conversion α (assuming $n \neq 1$)

$$\frac{(1-\alpha)^{1-n} - (1-\alpha_I)^{1-n}}{n-1} = k \cdot (t_\alpha - t_I) \quad \text{with} \quad k = A_0 \cdot e^{-E_a/RT} \qquad (10)$$

The numerical fitting was performed for SnO and Zn at three different temperatures (Fig. 9). The numerical resolutions for all the fittings were performed with Matlab® (Mathwork™) by minimization through the simplex-based Nelder–Mead algorithm (*fminsearch* function). In the case of zinc, the powder hydrolysis before steam injection was significant. Consequently, the conversion when steam injection was started was used as the initial conversion α_I in the depletion model (Eq. (10)). The values of n and A_0 that fit closely with the isothermal conversion curve in the reaction-controlled domain are listed in Table 2, and show good correlation with experiments only before the regime switch. Indeed, the chosen depletion model f is designed to nullify the conversional rate only when conversion is complete, whereas the obtained final hydrolysis conversions plateaued at 80% for SnO and 50% for Zn. This gave reaction orders of 1.9 ± 0.2 and 3.3 ± 0.3 for SnO and Zn, respectively.

Non-isothermal tests were then achieved to perform the whole kinetic analysis on the same powder sample, which thereby allowed reduction of experimental uncertainties.

3.2.2. *Non-isothermal kinetic experiments at different heating rates*

3.2.2.1. Iso-conversion model-free method. A model-free approach was applied in order to determine the activation energies that are independent of the model assumptions. A reaction model $f(\alpha)$ was then not required.

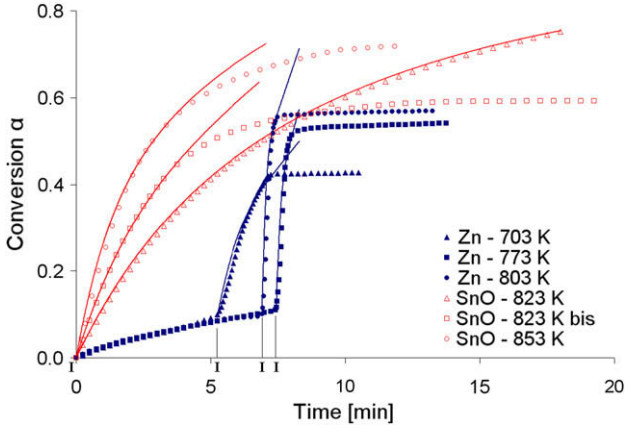

Fig. 9 – Isothermal hydrolysis data for SnO and Zn powders and results of the fitting from the empirical depletion model (lines, Eq. (10)).

Table 2 – Kinetic parameters identified from numerical fitting of Fig. 9 for isothermal hydrolysis data.

Temperature (K)	Reaction order, n	Pre-exponential factor, A_0 (10^2 s^{-1})
SnO powders ($E_a = 124$ kJ/mol)		
823	1.7	1600
823	1.7	2450
853	2.0	2200
Zn powders ($E_a = 87$ kJ/mol)		
703	3.0	200
773	3.3	320
803	3.6	270

Non-isothermal hydrolysis tests were performed at constant heating rates and the iso-conversion model-free method of Vyazovkin and Wight [24] was applied. If the reaction starts at T_I (water injection temperature) with constant heating rate β, sorting out and integrating Eq. (9) gives the following:

$$g(\alpha) = \int_0^\alpha \frac{d\alpha}{f(\alpha)} = A_0 \int_{t_I}^{t_\alpha} e^{-E_a/R(T_I+\beta t)}\, dt = \frac{A_0}{\beta} \int_{T_I}^{T_\alpha} e^{-E_a/RT}\, dT = J(E_a,\ \beta,\ T_\alpha) \qquad (11)$$

Assuming that f is not temperature-dependent, the left-side term $g(\alpha)$ is constant whatever be β, and so does the right-side term J. Consequently, for a given α and for different β_i, β_j, the J_i/J_j ratios should be equal to unity. In order to use a procedure that is independent of the number of experiments at n different β, the variance that should be null was used instead.

$$S^2(E_{a,\alpha}) = \frac{1}{n(n-1)} \sum_i^n \sum_{j \neq 1}^n \left[\frac{J_i}{J_j} - 1 \right]^2 \qquad (12)$$

Hence for each α, the activation energy $E_{a,\alpha}$ corresponds to the minimum of Eq. (12). It was found by numerical integration (trapezoidal rule) and by looking for the minimum E_a. Uncertainties were calculated according to the fact that the variance to the minimal variance ratio follows the F-distribution (assuming a 90% confidence range) [24].

The conversion curves of SnO hydrolysis carried out at three different β are shown in Fig. 6. Steam flow injection was started from the temperature at which the reactivity became noticeable ($T_I = 693$ K for SnO). As the linear heating of the furnace ended before the final conversion was reached, useful conversion data were limited to the 0–65% range. Fig. 10 shows that $E_{a,\alpha}$ is almost constant. By neglecting activation energies with high uncertainties, E_a was determined to be in the 120 ± 20 kJ/mol range.

In comparison, the Zn powder did not react completely even at the maximum temperature reached (Fig. 7) and the conversion reached a plateau. The activation energy calculated from the conversion data at 30% was 75 ± 20 kJ/mol. This is lower than that reported in previous studies for commercial zinc powders (132 ± 27 kJ/mol) [11]. These commercial powders contained trace metal impurities (in particular Cu, Mg, Ni, Ti). Zinc reactivity is driven by the diffusion of Zn^{2+} ions [14], and metal impurities may hinder ionic diffusion [25]. In contrast, the solar-produced zinc particles had a negligible content in trace metal impurities due to the phase change

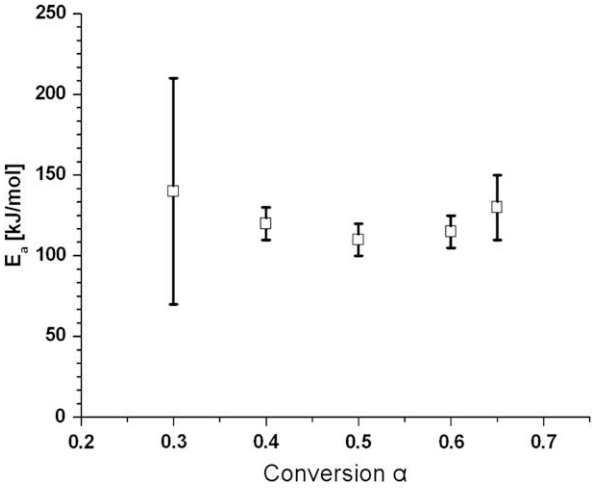

Fig. 10 – Activation energy versus conversion determined by the model-free method from the data of non-isothermal SnO hydrolysis.

during the solar ZnO reduction. The calculated E_a, however, was above that of pure zinc surfaces' hydrolysis (about 45 kJ/mol for both H_2O adsorption and reaction) [26,27]. This may be explained by the initial oxide layer at the surface of the solar-produced zinc nanoparticles (from the recombination reaction), which hinders diffusion and structural reorganizations [27]. As previously discussed in Ref. [14], the large discrepancies in activation energy for zinc hydrolysis given by various studies (from 43 to 145 kJ/mol) may also be owed to different particle size distributions [28].

The differences observed between the activation energies for solar-produced Zn and SnO powders could be explained by the stability of the activated species (hydrated Zn/SnO). Indeed, Pauling electronegativity of zinc is lower than that of tin, so this must be easier for zinc to share electrons. As SnO is more electron-depleted than metallic tin, it shares even less its electrons. Consequently, SnO is less ''attractive'' for H_2O than metallic zinc, which results in the favored formation of the H_2O–Zn complex over the H_2O–SnO one. By definition, this means that the activation energy of Zn hydrolysis should be lower than the SnO one.

This rigorous model-free method provided reference values of the activation energies for SnO and Zn powders hydrolysis. The ranges of uncertainty were determined. The identified values of activation energies were similar to the ones determined from the isothermal hydrolysis data and thus validated the methods. Overlapping of the uncertainty ranges for the previous methods (isothermal and model-free) allowed estimating the most probable values, 122 ± 13 kJ/mol for SnO and 87 ± 7 kJ/mol for Zn. These activation energies were then used to determine the reaction orders and pre-exponential factors of the hydrolysis reactions, still from the non-isothermal data.

3.2.2.2. *Empirical reaction model*. The empirical depletion model (Eq. (9)) with $f(\alpha) = (1-\alpha)^n$ was used again to identify the kinetic parameters from the non-isothermal hydrolysis tests at different heating rates β. A variable change was performed ($u = 1/T$), which gives the following:

$$\frac{d\alpha}{(1-\alpha)^n} = -\frac{A_0}{\beta} e^{(-E_a/R)u} \frac{du}{u^2} \tag{13}$$

As u is positive, the equation becomes

$$\frac{d\alpha}{(1-\alpha)^n} = -\frac{A_0}{\beta} e^{-((E_a/R)u + 2\ln u)}\, du \tag{14}$$

A second variable change with $v = (E_a/R) + 2\ln u$ gives $du = dv/Z(u)$ with $Z(u) = E_a/R + 2/u$, consequently

$$\frac{d\alpha}{(1-\alpha)^n} = -\frac{A_0}{\beta Z(u)} e^{-v}\, dv \tag{15}$$

For the Zn and SnO hydrolysis experiments represented in Figs. 11 and 12, and assuming E_a greater than 80 kJ/mol, $Z(u)$ varied less than 5% over the hydrolysis temperature ranges, whereas the exponential term changes were of several orders of magnitude. $Z(u)$ was thus assumed constant relative to the temperature and calculated at the average temperature $T_{1/2} = (T_{max} - T_I)/2$. Consequently, Eq. (15) was integrated analytically (assuming $n \neq 1$) resulting in the following:

$$\alpha = 1 - \left[1 + \frac{A_0(n-1)}{\left(\frac{E_a}{R} + 2T_{1/2}\right)\beta}\left(\exp\left(\frac{-E_a}{RT} - 2\ln\frac{1}{T}\right) - \exp\left(\frac{-E_a}{RT_0} - 2\ln\frac{1}{T_0}\right)\right)\right]^{1/(1-n)} \tag{16}$$

Numerical fittings of the hydrolysis results at constant β with Eq. (16) were performed by fixing the value of the activation energy (122 kJ/mol and 87 kJ/mol for SnO and Zn, respectively), because E_a and A_0 are partially coupled [29] and independent fitting of each parameter is thus not possible. The fitting was achieved by focusing on the first stage of the hydrolysis corresponding mostly to the reaction-controlled domain (Figs. 11 and 12). A satisfactory correlation was obtained with the fitted values of n and A_0 (Table 3). These values fairly agreed with those identified from the isothermal hydrolysis tests (Table 2), which means that the chosen depletion model $f(\alpha) = (1-\alpha)^n$ was appropriate. Furthermore, this proves that the results dependency on f_{wt} is not significant as various powders hydrolysis gave similar kinetic parameters. The significantly higher reaction order n for zinc means that zinc powder deactivation was quicker than for

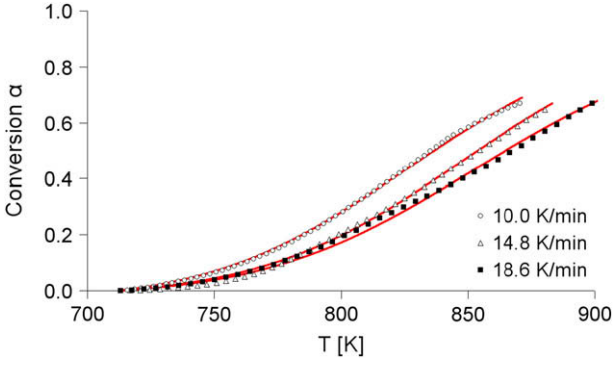

Fig. 11 – Hydrolysis of SnO powders at different heating rates and results of the fitting model (lines, Eq. (16)).

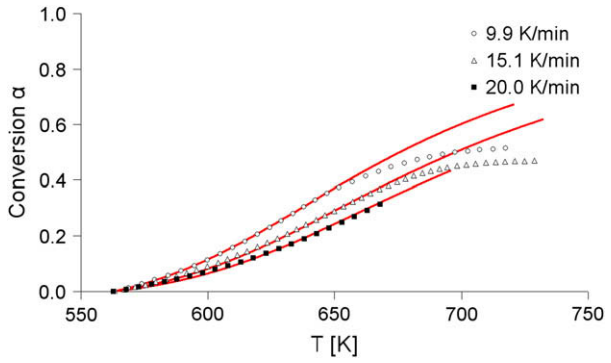

Fig. 12 – Hydrolysis of Zn powders at different heating rates and results of the fitting model (lines, Eq. (16)).

SnO. This deactivation was due to the ZnO shell at the particles surface, which explained the low final conversion (below 50%). A lower value of the reaction order was previously reported for Zn hydrolysis ($n = 1.6$) [11], and it may come from the high dispersion of the nanoparticles, decreasing the diffusion limitations. These diffusion-related issues were investigated in the case of SnO by applying a more physical approach based on the gas–solid shrinking core model.

3.2.3. *Shrinking core model applied to SnO hydrolysis*

The SnO hydrolysis was physically described with a gas–solid shrinking core model (SCM) [30]. This approach implies that the reaction order in the reaction-controlled regime (at the beginning of the reaction) must be equal to 2/3. This value corresponds to the particular case of a contracting sphere model (Eq. (9) with $f(\alpha) = (1-\alpha)^{2/3}$) and means that diffusion limitations are negligible (case of surface reaction). Instead, a reaction order of 2.0 ± 0.2 was identified for most of the SnO hydrolysis experiments with the previous empirical depletion model (Tables 2 and 3), which thus suggests that diffusion phenomena was occurring from the start of hydrolysis (as soon as the steam was injected). SCM assumes that a solid layer of SnO_2 grows at the surface of the reactive particles and causes diffusion limitations of the reactant (H_2O) to the core of SnO. The model considers spherical nanoparticles with uniform mean diameter, which means that the twin surfaces of the agglomerates are neglected. The solid–gas reaction can be described by successive limiting steps:

(a) external diffusion of H_2O from the gaseous phase to the particle surface,
(b) internal diffusion of H_2O from the surface to the core,
(c) first order reaction at the core surface.

Applying the SCM theory gives the integrated form of the rate equation

$$t = \tau_{de}\alpha + \tau_{di}\left[1 - 3(1-\alpha)^{2/3} + 2(1-\alpha)\right] + \tau_r\left[1 - (1-\alpha)^{1/3}\right] \quad (17)$$

where τ_{de}, τ_{di}, and τ_r are characteristic times (fitting parameters) for steps (a), (b), and (c), respectively.

Rigorously, the SCM model depends on the particles geometry (sphere, disk, cylinder), but only the model for spherical particles allowed good fitting of experimental results. The fitting results related to the beginning of SnO hydrolysis (chemical reaction control) are listed in Table 4. The external mass transfer (τ_{de}) is negligible because the steam is in excess. The regime is not completely controlled by intrinsic reaction at the front because the internal diffusion and intrinsic reaction parameters have the same order of magnitude. This internal diffusion limitation may be strengthened by the initial presence of a SnO_2 layer formed during the recombination with O_2 before hydrolysis.

The fitting parameters roughly decrease with temperature as expected. τ_r is inversely proportional to the kinetic constant that accounts for the intrinsic chemical reaction occurring at the reaction front

$$\tau_r = \frac{\rho_{SnO} \cdot r}{k \cdot C_{H_2O}} \quad (18)$$

where ρ_{SnO} is the molar density of SnO (true density to molar weight ratio: $48 \pm 1 \times 10^3$ mol/m^3) and r is the particle mean radius (50 nm). Assuming that only k and C_{H_2O} vary with the hydrolysis temperature, and that C_{H_2O} is inversely proportional to T (ideal gas law), then the kinetic parameters can be obtained by linear regression. The Arrhenius plot is shown in Fig. 13. The value of E_a (126 ± 14 kJ/mol, $R^2 = 96\%$) accounts for intrinsic reaction at the front only, and it is similar to the one from the model-free method, suggesting that diffusion in the initial SnO_2 layer has a negligible effect on the activation energy.

The same fitting procedure was repeated for the second part of the conversion curves corresponding to the end of the hydrolysis (diffusion-controlled regime). In that case, the fitting parameters (Table 5) indicate that the reaction is controlled predominantly by the diffusion of the reactants through the product layer rather than intrinsic chemical

Table 3 – Kinetic parameters retrieved from numerical fitting of Figs. 11 and 12 with Eq. (16) for non-isothermal hydrolysis data.

Heating rate, β (K/min)	Reaction order, n	Pre-exponential factor, A_0 (10^2 s^{-1})
SnO powders ($E_a = 122$ kJ/mol)		
10.0	2.0	1670
14.8	1.8	1540
18.6	2.1	1680
Zn powders ($E_a = 87$ kJ/mol)		
9.9	3.3	400
15.1	3.7	410
20.0	4.0	420

Table 4 – SCM parameters for hydrolysis of SnO related to chemical reaction control.

Temperature (K)	τ_{di} (±30%) (s)	τ_r (±10%) (s)
773	1240	3480
803	390	1240
823	1640	1200
823	1080	910
823	850	840
853	310	630

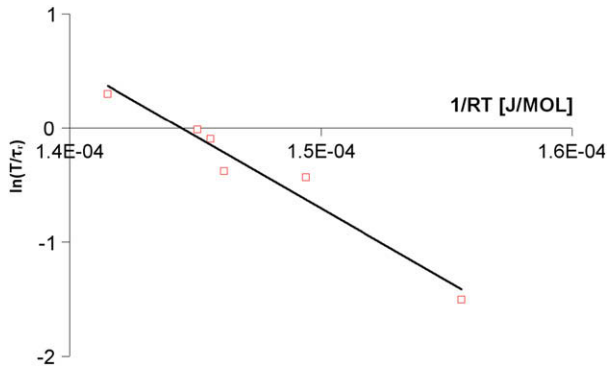

Fig. 13 – Arrhenius plot for the isothermal SnO hydrolysis experiments derived from the SCM model (Table 4), $E_a = 126 \pm 14$ kJ/mol ($R^2 = 96\%$).

reaction at the surface ($\tau_r = 0$). τ_{di} is inversely proportional to the diffusion coefficient of the gas through the growing layer of oxide

$$\tau_{di} = \frac{\rho_{SnO} r^2}{6 D_e C_{H_2O}} \quad (19)$$

where D_e is the equivalent diffusivity (m^2/s) of H_2O in the SnO_2 layer, meaning that this process encompasses all the occurring diffusion processes (molecular and ionic). For particles with radius ranging between 10 and 50 nm (according to XRD and SEM), this diffusivity is in the 10^{-18} to 10^{-15} m^2/s range. This is higher than the diffusivity of O_2 molecule in SnO_2, previously measured at similar temperatures (10^{-19} to 10^{-18} m^2/s at 793 K) [31]. This is also at least two orders of magnitude higher than Zn^{2+} ions diffusivity ($6.6–14.5 \times 10^{-20}$ m^2/s) [14], suggesting that diffusion processes are less limiting in SnO case. Aside from the model-related error, the high diffusivity for steam could be explained by some cracks in the diffusion layer, which may facilitate mass transfer inside the particles.

This SCM approach brought a further validation of the kinetic parameters from a physical model in the case of SnO. It was not applied to Zn because the numerical fitting of the zinc hydrolysis data with Eq. (17) was not possible. The hydrolysis of Zn particles is mainly controlled by the fast surface reaction step. The diffusion-controlled step is not observed because of the low-permeable ZnO layer formed at the particles surface. Thus, the shrinking core model is not suitable in the case of Zn.

Table 5 – SCM parameters for hydrolysis of SnO related to diffusion control.

Temperature (K)	τ_{de} (s)	τ_{di} (±30%) (s)
773	10	6170
803	10	2400
823	10	3700
823	10	5200
823	10	4700
853	10	1900

4. Conclusion

The ZnO/Zn and SnO_2/SnO two-step thermochemical cycles for H_2 production encompass the hydrolysis of Zn and SnO solar-produced nanoparticles. This study compared this hydrolysis step for both cycles, in which steam oxidation of Zn or SnO yields hydrogen. In the experimental study, a fixed-bed reactor layout was used and the reactor characteristics allowed the control of the heating rate and temperature, enabling determination of kinetic rate laws. The reacting nanoparticles were synthesized by solar thermal reduction of ZnO and SnO_2 and neutral gas quenching of the vapors. The qualitative differences in the hydrogen production profiles from Zn and SnO hydrolysis were first addressed and the maximum hydrogen yields were quantified. Although Zn hydrolysis was much faster than SnO hydrolysis, the final H_2 yield was lower for Zn than for SnO, resulting in similar H_2 productivities (about 6 mmol H_2 per gram of SnO_2 or ZnO). Then, the kinetic parameters for an uncoupled Arrhenius equation were determined. An empirical depletion model was applied to estimate the activation energy and reaction order for the hydrolysis of Zn and SnO solar-produced nanopowders

$$Ea = 122\ \text{kJ/mol} \quad \text{and} \quad n = 2 \quad \text{for SnO},$$

$$Ea = 87\ \text{kJ/mol} \quad \text{and} \quad n = 3.5 \quad \text{for Zn}.$$

Then, the activation energies were validated through a model-free method based on the hydrolysis data at different heating rates. Finally, the hydrolysis reaction of SnO nanoparticles was modeled by the solid–gas shrinking core approach to characterize more precisely the reaction-controlling phenomena. This study was the first detailed kinetic analysis for the hydrolysis of solar-produced Zn and SnO nanopowders. Larger powder samples will be synthesized with a new solar reactor operating continuously, which will then enable investigating the hydrolysis step with strictly the same reduced powder for every experiments.

Acknowledgments

We gratefully acknowledge the CNRS Department of Engineering and Information Science (ST2I) and the Languedoc-Roussillon Regional Council for their financial support. We also thank C. Rolland and A. Nzihou from EMAC (Albi, France) for SEM and ESEM characterization of reactant powders, and R. Garcia for the construction of the experimental set-up for solar synthesis of powders and hydrolysis tests.

REFERENCES

[1] Meng QY, Bentley RW. Global oil peaking: responding to the case for 'abundant supplies of oil'. Energy 2008;33(8):1179–84.
[2] Marbán G, Valdés-Solís T. Towards the hydrogen economy? Int J Hydrogen Energy 2007;32(12):1625–37.
[3] Funk JE. Thermochemical hydrogen production: past and present. Int J Hydrogen Energy 2001;26(3):185–90.

[4] Steinfeld A. Solar thermochemical production of hydrogen – a review. Solar Energy 2005;78(5):603–15.
[5] Bilgen E, Ducarroir M, Foex M, Sibieude F, Trombe F. Use of solar energy for direct and two-step water decomposition cycles. Int J Hydrogen Energy 1977;2(3):251–7.
[6] Palumbo R, Lédé J, Boutin O, Elorza Ricart E, Steinfeld A, Möller S, et al. The production of Zn from ZnO in a high-temperature solar decomposition quench process – I. The scientific framework for the process. Chem Eng Sci 1998; 53(14):2503–17.
[7] Weidenkaff A, Steinfeld A, Wokaun A, Auer PO, Eichler B, Reller A. Direct solar thermal dissociation of zinc oxide: condensation and crystallization of zinc in the presence of oxygen. Solar Energy 1999;65(1):59–69.
[8] Berman A, Epstein M. The kinetics of hydrogen production in the oxidation of liquid zinc with water vapor. Int J Hydrogen Energy 2000;25(10):957–67.
[9] Weidenkaff A, Reller AW, Wokaun A, Steinfeld A. Thermogravimetric analysis of the ZnO/Zn water splitting cycle. Thermochim Acta 2000;359(1):69–75.
[10] Vishnevetsky I, Epstein M. Production of hydrogen from solar zinc in steam atmosphere. Int J Hydrogen Energy 2007;32(14): 2791–802.
[11] Funke HH, Diaz H, Liang X, Carney CS, Weimer AW, Li P. Hydrogen generation by hydrolysis of zinc powder aerosol. Int J Hydrogen Energy 2008;33(4):1127–34.
[12] Wegner K, Ly HC, Weiss RJ, Pratsinis SE, Steinfeld A. In situ formation and hydrolysis of Zn nanoparticles for H_2 production by the 2-step ZnO/Zn water-splitting thermochemical cycle. Int J Hydrogen Energy 2006;31(1): 55–61.
[13] Melchior T, Piatkowski N, Steinfeld A. H_2 production by steam-quenching of Zn vapor in a hot-wall aerosol flow reactor. Chem Eng Sci 2009;64:1095–101.
[14] Ernst FO, Steinfeld A, Pratsinis SE. Hydrolysis rate of submicron Zn particles for solar H_2 synthesis. Int J Hydrogen Energy 2009;34:1166–75.
[15] Abanades S, Charvin P, Flamant G, Neveu P. Screening of water-splitting thermochemical cycles potentially attractive for hydrogen production by concentrated solar energy. Energy 2006;31(14):2469–86.
[16] Charvin P, Abanades S, Lemort F, Flamant G. Experimental study of SnO_2/SnO/Sn thermochemical systems for solar production of hydrogen. AIChE J 2008;54(10):2759–67.
[17] Abanades S, Charvin P, Lemort F, Flamant G. Novel two-step SnO_2/SnO water-splitting cycle for solar thermochemical production of hydrogen. Int J Hydrogen Energy 2008;33(21): 6021–30.
[18] Souriau D. Procédé et dispositif pour l'utilisation d'énergie thermique à haute température, en particulier d'origine nucléaire. [Device and method for the use of high-temperature heat energy, in particular of nuclear origin]. Gaz de France 1972. Patent FR2135421 [in French].
[19] Vishnevetsky I, Epstein M. Tin as a possible candidate for solar thermochemical redox process for hydrogen production. In: Proceedings of ES2007. Long Beach, California; June 27–30, 2007. New York: ASME.
[20] Jenkins R, Snyder R. Introduction to X-ray powder diffractometry. New York, NY: John Wiley and Sons, Inc.; 1996.
[21] Kouam J, Ait-Ahcene T, Plaiasu AG, Abrudeanu M, Motoc A, Beche E, et al. Characterization and properties of ZnO based nanopowders prepared by solar physical vapor deposition (SPVD). Solar Energy 2008;82(3):226–38.
[22] Dai ZR, Gole JL, Stout JD, Wang ZL. Tin oxide nanowires, nanoribbons, and nanotubes. J Phys Chem B 2002;106(6): 1274–9.
[23] Iwanaga H, Fujii M, Ichihara M, Takeuchi S. Some evidence for the octa-twin model of tetrapod ZnO. J Cryst Growth 1994; 141(1):234–8.
[24] Vyazovkin S, Wight CA. Estimating realistic confidence intervals for the activation energy determined from thermoanalytical measurements. Anal Chem 2000;72(14): 3171–5.
[25] Tomlins GW, Routbort JL, Mason TO. Zinc self-diffusion, electrical properties, and defect structure of undoped, single crystal oxide. J Appl Phys 2000;87(1):117–23.
[26] Bazán JC, Gschaider ME, Alimenti GA. Gravimetric study of interaction of water vapor with metallic zinc. J Therm Anal Calorim 1999;55(2):569–79.
[27] Alimenti GA, Gschaider ME, Bazán JC, Ferreira ML. Theoretical and experimental study of the interaction of O_2 and H_2O with metallic zinc – discussion of the initial step of oxide formation. J Colloid Interface Sci 2004;276(1):24–38.
[28] Park K, Lee D, Rai A, Mukherjee D, Zachariah MR. Size resolved kinetic measurements of aluminum nanoparticle oxidation with single particle mass spectrometry. J Phys Chem B 2005;109(15):7290–9.
[29] Eisenreich N. Direct least squares fit of chemical reaction curves and its relation to the kinetic compensation effect. J Therm Anal 1980;19(2):289–96.
[30] Levenspiel O. Chemical reaction engineering. New York, NY: John Wiley and Sons, Inc.; 1999.
[31] Hellmich W, Bosch-v Ch, Müller G, Sberveglieri G, Berti M, Perego C. The kinetics of formation of gas-sensitive RGTO–SnO_2 films. Thin Solid Films 1995;263(2):231–7.